

# SCIENTIFIC REPORTS



OPEN

## Fe-based hybrid electrocatalysts for nonaqueous lithium-oxygen batteries

Seun Lee<sup>1</sup>, Gwang-Hee Lee<sup>1</sup>, Hack Jun Lee<sup>1</sup>, Mushtaq Ahmad Dar<sup>2</sup> & Dong-Wan Kim<sup>1</sup>

Lithium–oxygen batteries promise high energy densities, but are confronted with challenges, such as high overpotentials and sudden death during discharge–charge cycling, because the oxygen electrode is covered with the insulating discharge product,  $\text{Li}_2\text{O}_2$ . Here, we synthesized low-cost Fe-based nanocomposites via an electrical wire pulse process, as a hybrid electrocatalyst for the oxygen electrode of Li– $\text{O}_2$  batteries.  $\text{Fe}_3\text{O}_4$ -Fe nanohybrids-containing electrodes exhibited a high discharge capacity ( $13,890 \text{ mA h g}_c^{-1}$  at a current density of  $500 \text{ mA g}_c^{-1}$ ), long cycle stability (100 cycles at a current rate of  $500 \text{ mA g}_c^{-1}$  and fixed capacity regime of  $1,000 \text{ mA h g}_c^{-1}$ ), and low overpotential (1.39V at 40 cycles). This superior performance resulted from the good electrical conductivity of the Fe metal nanoparticles during discharge–charge cycling, which could enhance the oxygen reduction reaction and oxygen evolution reaction activities. We have demonstrated the increased electrical conductivity of the  $\text{Fe}_3\text{O}_4$ -Fe nanohybrids using electrochemical impedance spectroscopy.

Transition metal oxides (TMOs) are effective catalysts in various fields, such as water splitting<sup>1</sup>, fuel cells<sup>2</sup>, wastewater treatment<sup>3</sup>, biomedical applications, and energy storage<sup>4–6</sup> as electrocatalysts, TMOs enable rechargeable batteries with high energy densities, for use in the energy storage systems of smart grids and electric vehicles. TMO electrocatalysts are one of the key technologies in the area of lithium–oxygen (Li– $\text{O}_2$ ) batteries<sup>7–10</sup>. Li– $\text{O}_2$  batteries are confronted by several critical problems, including a high overpotential during discharge–charge cycling, low rate capability, and capacity fading owing to the sluggish kinetics of the oxygen reduction reaction (ORR) and oxygen evolution reaction (OER) during discharge and charge cycling<sup>11–13</sup>. In particular, during the discharge process, the oxygen electrode is covered with  $\text{Li}_2\text{O}_2$ , which is intrinsically electronically insulating and does not provide the electrodes with sufficient electronic conductivity, resulting in sudden death<sup>14,15</sup>. As a result, Li– $\text{O}_2$  batteries have capacity limitations. Therefore, electrocatalysts should be developed to significantly improve reversibility.

Among the TMO candidates,  $\text{Fe}_3\text{O}_4$  is considered a promising electrocatalyst owing to its high abundance, low cost, and excellent catalytic performance, which is better than that of other TMOs<sup>16–19</sup>.  $\text{Fe}_3\text{O}_4$  has good electronic conductivity and excellent catalytic activity for oxygen reduction due to continuous electron exchange between the octahedrally coordinated Fe(II) and Fe(III) positions via electron hopping<sup>20</sup>. However, although numerous recent studies on TMO electrocatalysts have exhibited improved cycle performance, the effect of the electrochemical performance derived from  $\text{Fe}_3\text{O}_4$  on the oxygen electrodes for Li– $\text{O}_2$  batteries has been rarely reported<sup>21–23</sup>.

Previous reports suggest that metal or carbon based iron oxide nanocomposites prepared the highly active electrocatalyst in the Li– $\text{O}_2$  batteries<sup>23–25</sup>.  $\text{Fe}_3\text{O}_4$ /Fe core-shell electrocatalysts for Li– $\text{O}_2$  batteries were uniformly dispersed on the surface of the carbon support, with the porous structure of carbon well persevered and high catalytic activity towards the ORR and OER<sup>23</sup>. However, it is still a challenge to design electrocatalysts that can drastically improve the efficiency and cycling ability of current Li– $\text{O}_2$  batteries.

Herein, we report a facile method for obtaining  $\text{Fe}_3\text{O}_4$ -Fe nanohybrids via an electrical wire pulse process. The  $\text{Fe}_3\text{O}_4$ -Fe nanohybrids showed excellent catalytic activity for both the ORR and OER during discharge–charge cycling. The obtained  $\text{Fe}_3\text{O}_4$ -Fe nanohybrids exhibited enhanced catalytic activity relative to  $\text{Fe}_3\text{O}_4$  nanospheres and manifested superior electrode performance, including a high specific capacity ( $13,890 \text{ mA h g}_c^{-1}$  at  $500 \text{ mA}$

<sup>1</sup>School of Civil, Environmental and Architectural Engineering, Korea University, Seoul, 02841, Republic of Korea.

<sup>2</sup>Center of Excellence for Research in Engineering Materials, Advanced Manufacturing Institute, College of Engineering, King Saud University, Riyadh, 11421, Saudi Arabia. Seun Lee and Gwang-Hee Lee contributed equally to this work. Correspondence and requests for materials should be addressed to D.-W.K. (email: [dwkim1@korea.ac.kr](mailto:dwkim1@korea.ac.kr))

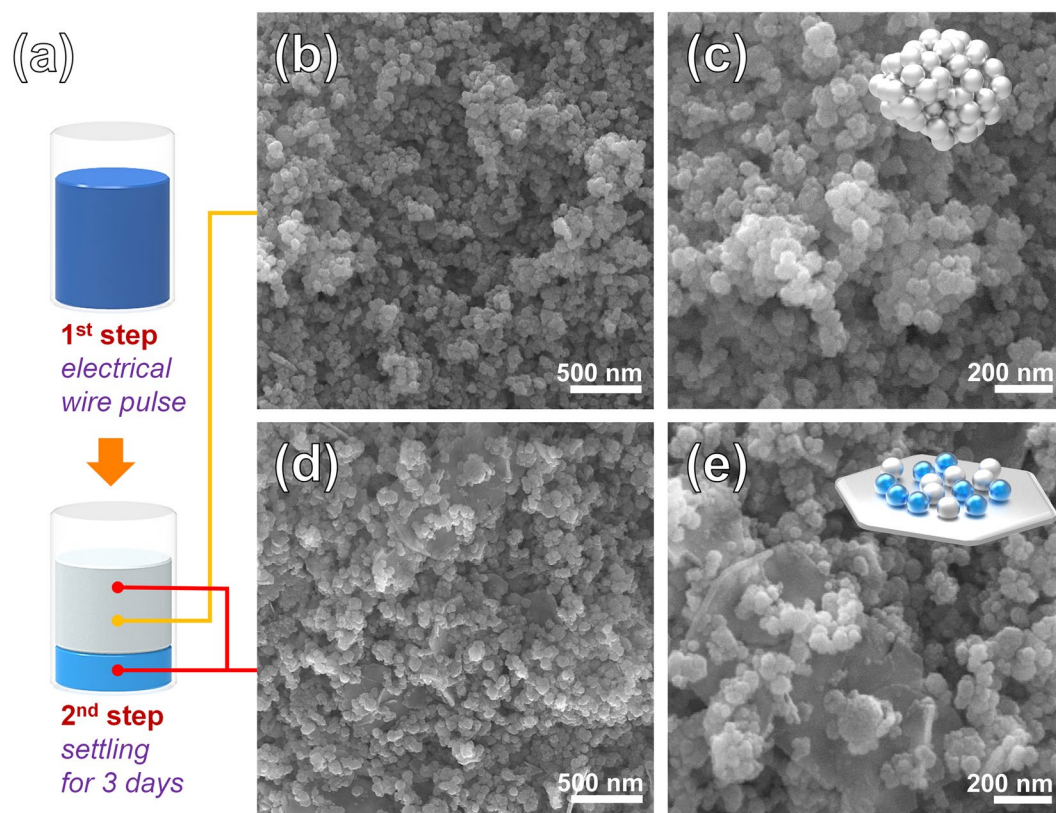


**Figure 1.** Morphology analysis of the  $\text{Fe}_3\text{O}_4$  nanospheres and the  $\text{Fe}_3\text{O}_4$ -Fe nanohybrids. (a) Scheme illustration of selection process of the  $\text{Fe}_3\text{O}_4$  nanospheres and the  $\text{Fe}_3\text{O}_4$ -Fe nanohybrids. FESEM images of (b,c) the  $\text{Fe}_3\text{O}_4$  nanospheres and (d,e) the  $\text{Fe}_3\text{O}_4$ -Fe nanohybrids.

$\text{g}_c^{-1}$ ), low overpotential (1.39 V at  $500 \text{ mA g}_c^{-1}$ ), and excellent high rate stability (150 cycles at  $2,000 \text{ mA g}_c^{-1}$  with a fixed capacity regime of  $1,000 \text{ mA h g}_c^{-1}$ ).

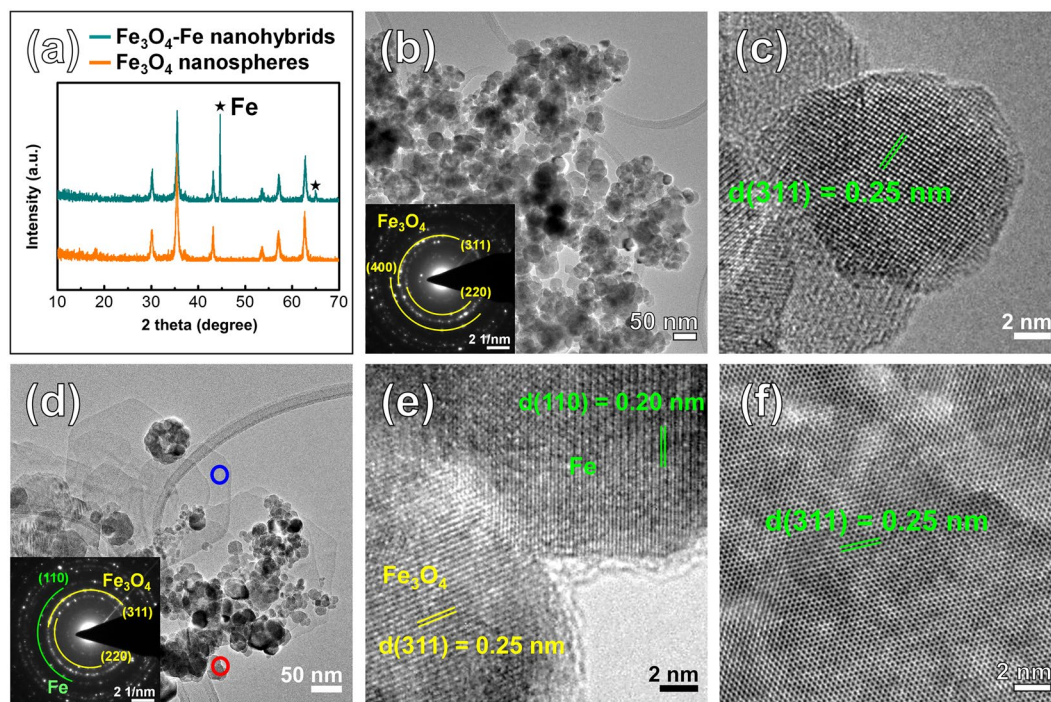
## Results and Discussion

Figure 1 shows a schematic of the selection process and typical field emission scanning electron microscopy (FESEM) images of the products obtained using the electrical wire pulse method. After the selection step, in which the suspension was allowed to settle, two different morphologies were obtained (Fig. 1b–e). After settling for 3 days, Fig. 1b and c show typical FESEM images of the  $\text{Fe}_3\text{O}_4$  nanospheres obtained from the upper-colloid solution, which have with very homogeneous shapes. Figure 1d and e show typical FESEM images of the  $\text{Fe}_3\text{O}_4$ -Fe nanohybrids obtained from the whole colloid solution, which have nanospheres as well as thin nanoflakes.

The crystal structures of the  $\text{Fe}_3\text{O}_4$  nanospheres and the  $\text{Fe}_3\text{O}_4$ -Fe nanohybrids were recorded using XRD, as shown in Fig. 2a. The X-ray diffraction (XRD) pattern of the  $\text{Fe}_3\text{O}_4$  nanospheres can be indexed to cubic  $\text{Fe}_3\text{O}_4$  (PDF card No. 88-0315). No signals from other impurities could be clearly detected, indicating that a high purity magnetite sample was prepared from the upper-colloid solution after settling. The XRD pattern of the  $\text{Fe}_3\text{O}_4$ -Fe nanohybrids had diffraction peaks that were similar to those of the  $\text{Fe}_3\text{O}_4$  nanospheres. In addition, new diffraction peaks at  $44.7^\circ$  and  $65^\circ$  were observed, which could be attributed to cubic Fe (PDF card No. 06-0696).

To further confirm the morphology and structure of the  $\text{Fe}_3\text{O}_4$  nanospheres and the  $\text{Fe}_3\text{O}_4$ -Fe nanohybrids, TEM images were obtained, as shown in Fig. 2b–f. Figure 2b and c show typical transmission electron microscopy (TEM) images of the  $\text{Fe}_3\text{O}_4$  nanospheres, with a similar morphology to that observed by SEM. The  $\text{Fe}_3\text{O}_4$  nanospheres had diameters of less than 50 nm and were aggregated with an approximately spherical shape. The selected area electron diffraction (SAED) pattern demonstrates the highly crystalline nature of the nanoparticles (inset of Fig. 2b). The lattice spacing, calculated based on the electron diffraction patterns, are in agreement with that of cubic  $\text{Fe}_3\text{O}_4$  (PDF card No. 88-0315). The high-resolution TEM (HRTEM) image in Fig. 2c shows that the inter-planar distance in the  $\text{Fe}_3\text{O}_4$  nanospheres is 0.25 nm, which is consistent with the (311) plane of cubic  $\text{Fe}_3\text{O}_4$ .

The TEM images of the  $\text{Fe}_3\text{O}_4$ -Fe nanohybrids reveal 0D spheres deposited on 2D flake composites (Fig. 2d). The SAED pattern of the nanocomposites can be indexed to cubic  $\text{Fe}_3\text{O}_4$  (PDF card No. 88-0315) and cubic Fe (PDF card No. 06-0696), which is consistent with the XRD results. Figure 2e shows the HRTEM image of a selected nanosphere in Fig. 2d (indicated by the red circle), and reveals the presence of two different types of nanospheres. The inter-planar distance of 0.25 nm corresponds to the (311) plane of  $\text{Fe}_3\text{O}_4$ , whereas the other region with an inter-planar distance of 0.20 nm is indexed to the (110) plane of Fe. The energy-dispersive X-ray spectroscopy (EDS) mapping profile of the  $\text{Fe}_3\text{O}_4$ -Fe nanohybrids, as shown in Supplementary Fig. S1, indicating that Fe and O elements are respectively populated in the  $\text{Fe}_3\text{O}_4$ -Fe nanohybrids. Supplementary Fig. S1b show the



**Figure 2.** Structure and component analysis of the  $\text{Fe}_3\text{O}_4$  nanospheres and the  $\text{Fe}_3\text{O}_4$ -Fe nanohybrids. (a) XRD patterns of  $\text{Fe}_3\text{O}_4$  nanospheres and the  $\text{Fe}_3\text{O}_4$ -Fe nanohybrids. (b) Low-magnification TEM images and SAED pattern (inset) and (c) HRTEM image of the  $\text{Fe}_3\text{O}_4$  nanospheres. (d) Low-magnification TEM images and SAED pattern (inset) of the  $\text{Fe}_3\text{O}_4$ -Fe nanohybrids, and (e) HRTEM image of the nanosphere indicated by red circle of (d), (f) HRTEM image of the nanoflake indicated by blue circle of (d).

EDS element color mixing mapping of the  $\text{Fe}_3\text{O}_4$ -Fe nanohybrids. The element mapping images in Supplementary Fig. S1b–d reveal the presence of O (purple) and Fe (yellow) elements, as determined from the EDS analysis. The Fe nanospheres are evenly distributed in the  $\text{Fe}_3\text{O}_4$ -Fe nanohybrids (Supplementary Table S1). Figure 2f shows the HRTEM image of a selected nanoflake in Fig. 2d (indicated by the blue circle), and reveals the highly crystalline nature of the nanoflakes. The inter-planar distance of the nanoflakes is 0.25 nm, consistent with the (311) plane of cubic  $\text{Fe}_3\text{O}_4$ . The folded edge or protuberant ridge of the  $\text{Fe}_3\text{O}_4$  nanoflakes (see Supplementary Fig. S2a) demonstrate an average thickness of approximately 10 nm, suggesting that the nanoflakes comprise octahedral  $\text{Fe}_3\text{O}_4$  arranged with hexagonal symmetry in the planar direction. The  $\text{Fe}_3\text{O}_4$  flakes are laterally grown with cracked surfaces, as shown in Supplementary Fig. S2b. As this result, the surface of the  $\text{Fe}_3\text{O}_4$  nanoflakes can be expected to cause defects. So we measured surface chemistry using O 1s XPS analysis (Supplementary Fig. S3). Comparing the  $\text{Fe}_3\text{O}_4$ -Fe nanohybrids and the  $\text{Fe}_3\text{O}_4$  nanoflakes of O 1s XPS spectra, the O 1s peak of the  $\text{Fe}_3\text{O}_4$ -Fe nanohybrids is lower binding energy than that of the  $\text{Fe}_3\text{O}_4$  nanospheres. Shift of the O 1s peak to lower binding energy indicates oxygen vacancy<sup>26</sup>. Oxygen vacancy generated the charge of the defect state, which can be expected to have vigorous electrocatalytic activity.

The  $\text{Fe}_3\text{O}_4$  nanoflakes can be achieved by oriented attachment growth. The oriented attachment growth is contributed to reduce the overall energy of the formed  $\text{Fe}_3\text{O}_4$  nanocrystals. In other words, when the growth of  $\text{Fe}_3\text{O}_4$  seeds through a kinetically controlled process ceases, the 2D hexagonal flakes grow into more thermodynamically favored shape according to different surface facets of different surface energy<sup>27, 28</sup>.  $\text{Fe}_3\text{O}_4$  has a cubic inverse spinel structure which consists of a face-centered-cubic (FCC) close-packed structure with oxygen anions. As a FCC close-packed structure, the surface energies corresponding to different surface facets usually increase in the order of  $\gamma_{\{111\}} < \gamma_{\{100\}} < \gamma_{\{110\}}$ . In this crystal structure, the  $\text{Fe}_3\text{O}_4$  crystals usually exist with {111} planes as the basal surfaces.

In the electrical wire pulse method, when a high rate of energy is injected by a pulse with a high-density current, the fine metal wire is heated in a liquid solvent, and the generated energy leads to evaporation and condensation of the metal as a highly dispersed nanocolloids. The nanocolloids quickly grow through vapor cooling in the solvent<sup>29, 30</sup>. In case of our work, the oriented attachment growth would occur to form hexagonal  $\text{Fe}_3\text{O}_4$  nanoflakes at early growth stage by rapid hot-injection provided from a pulse with a high-density current. At high temperature, high energy facets will lead to a fast growth rate compared to low energy facets. During rapid pulsed explosion process, the  $\text{Fe}_3\text{O}_4$  nanospheres and the  $\text{Fe}_3\text{O}_4$ -Fe nanohybrids are produced because of repeated energy injection. As can be seen in Supplementary Fig. S4, typical TEM images of the  $\text{Fe}_3\text{O}_4$ -Fe nanohybrids are observed the attachments between aggregated particles, even larger ones. A hexagonal shaped aggregate can be seen being formed by the aggregation step (Supplementary Fig. S4a). This aggregated particles will continue to undergo oriented attachment growth to form a polycrystalline structure and subsequent recrystallization to a single crystal since the low surface energy of the {111} facet can no longer compensate for excessive strain energy



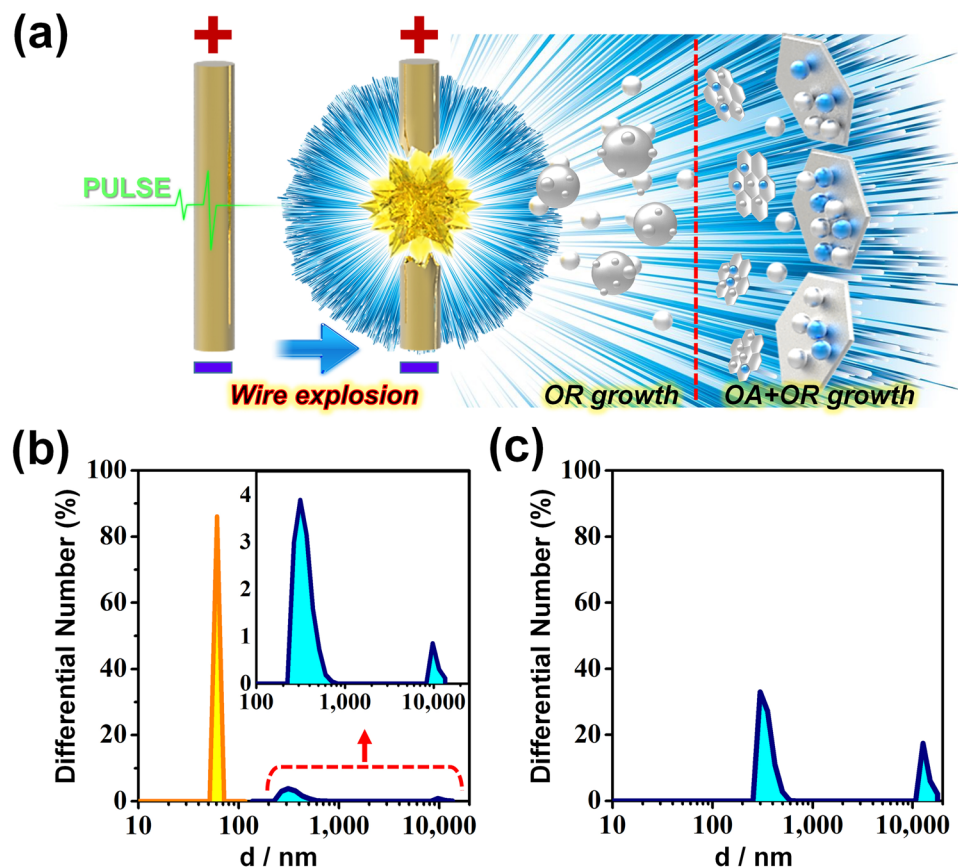


**Figure 3.** (a) Schematic illustration of growth mechanism of the Fe<sub>3</sub>O<sub>4</sub>-Fe nanohybrids (oriented attachment (OA) + Oswald ripening (OR) growth) and Fe<sub>3</sub>O<sub>4</sub> nanospheres (OR growth) by the electrical wire pulse process. Particle size distribution of (b) the Fe<sub>3</sub>O<sub>4</sub>-Fe nanohybrids and (c) the Fe<sub>3</sub>O<sub>4</sub> nanospheres.

(Supplementary Fig. S4b). Actually, both the oriented attachment growth and Oswald ripening occur simultaneously<sup>31,32</sup>. In the early growth stages of hot-injection, the strong surface adsorption lead to the oriented attachment growth, and the Oswald ripening is thermodynamically disturbed. Consequently, in later growth stage, large Fe<sub>3</sub>O<sub>4</sub> nanospheres and Fe<sub>3</sub>O<sub>4</sub> nanoflakes are formed by the Oswald ripening.

The particle size distribution of the Fe<sub>3</sub>O<sub>4</sub>-Fe nanohybrids and Fe<sub>3</sub>O<sub>4</sub> nanospheres can be obtained by dynamic light scattering analysis after adequate ultrasonic treatment. We observed three peaks for the Fe<sub>3</sub>O<sub>4</sub>-Fe nanohybrids around 60 nm, 310 nm, and 9 μm (Fig. 3b). However, the hydrodynamic diameters of the Fe<sub>3</sub>O<sub>4</sub> nanospheres were concentrated at 300 nm and 12 μm, with no peak around 60 nm (Fig. 3c). Because of the good dispersibility of the Fe<sub>3</sub>O<sub>4</sub> nanoflakes, it is assumed that the hydrodynamic diameters of the Fe<sub>3</sub>O<sub>4</sub>-Fe nanohybrids are concentrated at 60 nm. After settling for 3 days, the Fe<sub>3</sub>O<sub>4</sub> nanospheres were obtained from the upper-colloid solution. In contrast, the Fe<sub>3</sub>O<sub>4</sub>-Fe nanohybrids, which are both Fe<sub>3</sub>O<sub>4</sub> and Fe nanospheres deposited on the Fe<sub>3</sub>O<sub>4</sub> nanoflakes, sank to the lower-colloid solution owing to the different densities of Fe (7.9 g cm<sup>-3</sup>) and Fe<sub>3</sub>O<sub>4</sub> (5.2 g cm<sup>-3</sup>) (see Supplementary Table S2).

In this work, we tested Li-O<sub>2</sub> batteries with an oxygen electrode as the cathode, which consisted of Super P carbon black (SP) and the Fe<sub>3</sub>O<sub>4</sub>-Fe nanohybrids or Fe<sub>3</sub>O<sub>4</sub> nanospheres as electrocatalysts (weight ratio of 1:1). The first galvanostatic discharge-charge cycle of the Fe<sub>3</sub>O<sub>4</sub>-Fe nanohybrid-containing electrode (Fe<sub>3</sub>O<sub>4</sub>-Fe NH electrode) and the Fe<sub>3</sub>O<sub>4</sub> nanosphere-containing electrode (Fe<sub>3</sub>O<sub>4</sub> NS electrode) are shown in Fig. 4a at a current rate of 500 mA g<sub>c</sub><sup>-1</sup> (equivalent to 500 mA g<sub>electrocatalyst</sub><sup>-1</sup>). The most significant result was observed on cycling in the 2.0–4.8 V window. The Fe<sub>3</sub>O<sub>4</sub>-Fe NH electrode exhibited a discharge capacity of approximately 13,890 mA h g<sub>c</sub><sup>-1</sup>, which was superior to that of the Fe<sub>3</sub>O<sub>4</sub> NS electrode (10,680 mA h g<sub>c</sub><sup>-1</sup>). The morphological changes after discharge and charge at a current rate of 500 mA g<sub>c</sub><sup>-1</sup> for the Fe<sub>3</sub>O<sub>4</sub>-Fe NH and Fe<sub>3</sub>O<sub>4</sub> NS electrodes are shown in Supplementary Fig. S5. After discharge process, ORR aggregates (Li<sub>2</sub>O<sub>2</sub>) were covered fully on surface of the Fe<sub>3</sub>O<sub>4</sub>-Fe NH electrode (Supplementary Fig. S5a). The ORR aggregates disappeared at the end of the charge process (Supplementary Fig. S5b), indicating the high reversibility of the Fe<sub>3</sub>O<sub>4</sub>-Fe NH electrode. However, the Fe<sub>3</sub>O<sub>4</sub> NS electrode after discharge process are formed toroidal shaped ORR aggregates and were covered incompletely (Supplementary Fig. S5c). At the end of the charge process, the ORR aggregates were not fully decomposed (Supplementary Fig. S5d). The Fe<sub>3</sub>O<sub>4</sub> NS electrode indicates to operate the irreversible discharge-charge process.

The cyclic voltammograms (CV) for the Fe<sub>3</sub>O<sub>4</sub>-Fe NH and Fe<sub>3</sub>O<sub>4</sub> NS electrodes are shown in Supplementary Fig. S6. Both the anodic and cathodic peaks for the Fe<sub>3</sub>O<sub>4</sub>-Fe NH electrode were significantly larger than those for the Fe<sub>3</sub>O<sub>4</sub> NS electrode over five cycles. These results demonstrate the promising ORR/OER activity of the

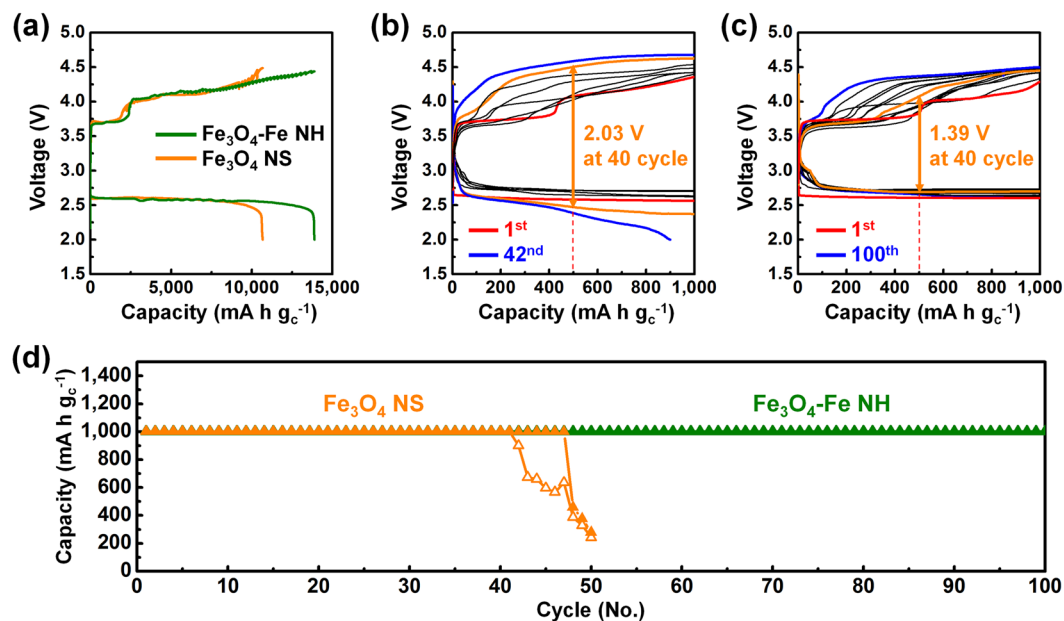


**Figure 4.** Electrochemical performances of the  $\text{Fe}_3\text{O}_4\text{-Fe NH}$  and the  $\text{Fe}_3\text{O}_4\text{ NS}$  electrode at a current rate of  $500\text{ mA g}^{-1}$ . **(a)** Galvanostatic discharge-charge curves for the  $\text{Fe}_3\text{O}_4\text{-Fe NH}$  electrode and the  $\text{Fe}_3\text{O}_4\text{ NS}$  electrode. **(b)** The  $\text{Fe}_3\text{O}_4\text{ NS}$  electrode and **(c)** the  $\text{Fe}_3\text{O}_4\text{-Fe NH}$  electrode at a fixed capacity regime of  $1,000\text{ mA h g}^{-1}$  with a rate of  $500\text{ mA g}^{-1}$ , **(d)** Comparison of the discharge-charge specific capacity versus the cycle number of the  $\text{Fe}_3\text{O}_4\text{-Fe NH}$  electrode and the  $\text{Fe}_3\text{O}_4\text{ NS}$  electrodes.

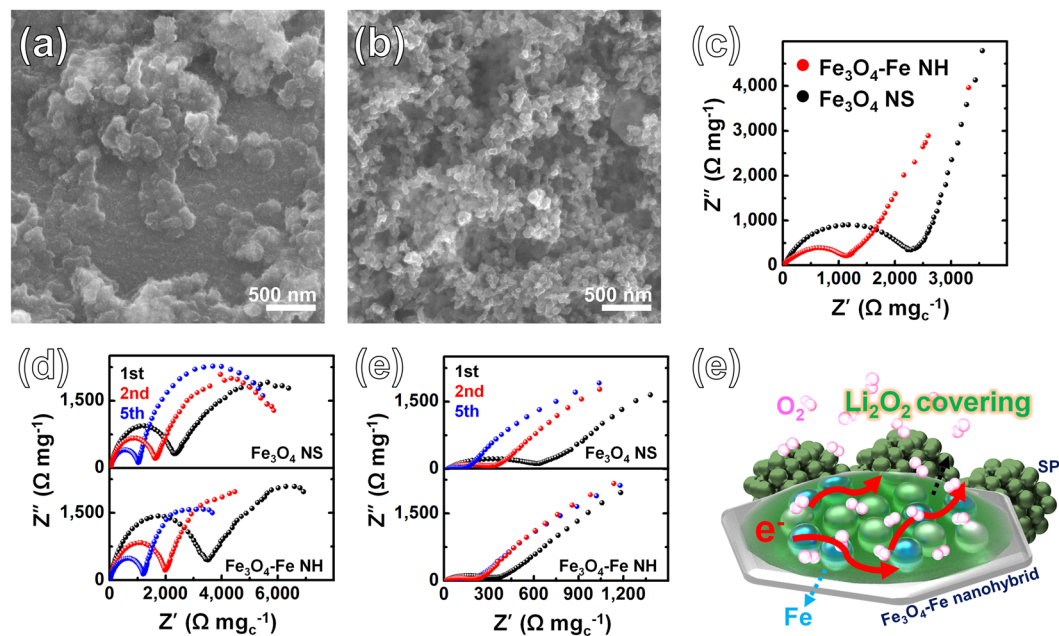
$\text{Fe}_3\text{O}_4\text{-Fe NH}$  electrode as an electrocatalyst in the  $\text{Li-O}_2$  battery. The peak above  $4.15\text{ V}$  in the first charge process likely corresponds to the decomposition of the carbon-containing electrolyte. The peak of the  $\text{Fe}_3\text{O}_4\text{ NS}$  electrode is obviously higher than that of the  $\text{Fe}_3\text{O}_4\text{-Fe NH}$  electrode, which should be related to the poor cycle reversibility<sup>33,34</sup>.

Figure 4b–d show the galvanostatic discharge-charge cycle performance of  $\text{Li-O}_2$  cells with the  $\text{Fe}_3\text{O}_4\text{-Fe NH}$  and  $\text{Fe}_3\text{O}_4\text{ NS}$  electrodes at a current rate of  $500\text{ mA g}^{-1}$  and at a fixed capacity regime of  $1,000\text{ mA h g}^{-1}$ . As can be seen Fig. 4c, the first voltage plateau of the  $\text{Fe}_3\text{O}_4\text{-Fe NH}$  electrode is around  $3.75\text{ V}$ . The second voltage plateau jumps suddenly to around  $4.00\text{ V}$  but remains relatively stable, reaching  $4.29\text{ V}$  at the end of the charging process. Ganpathy *et al.* observed two  $\text{Li}_2\text{O}_2$  oxidation stage during charge process<sup>35</sup>. At low voltage plateau, the amorphous  $\text{Li}_2\text{O}_2$  is decomposed, whereas at high voltage plateau, crystalline  $\text{Li}_2\text{O}_2$  is decomposed starting with the smaller crystals that evolves oxygen via a Li deficient solid-solution reaction. The overpotential of the  $\text{Fe}_3\text{O}_4\text{-Fe NH}$  electrode is lower than that of the  $\text{Fe}_3\text{O}_4\text{ NS}$  electrode during discharge-charge cycling. The galvanostatic discharge-charge curve of the  $\text{Fe}_3\text{O}_4\text{-Fe NH}$  electrode at 40 cycles (Fig. 4c) revealed a remarkably low overpotential ( $1.39\text{ V}$ ) compared with that of the  $\text{Fe}_3\text{O}_4\text{ NS}$  electrode ( $2.03\text{ V}$ ) (Fig. 4b). Indeed, the  $\text{Fe}_3\text{O}_4\text{-Fe NH}$  electrode could effectively enhance the electrocatalyst kinetics over 100 cycles (Fig. 4d).

To further investigate the enhanced electrocatalyst kinetics, we employed *ex-situ* FESEM after discharge-charge cycling and EIS analysis. The morphological changes after discharge and charge at a current rate of  $500\text{ mA g}^{-1}$  for the  $\text{Fe}_3\text{O}_4\text{-Fe NH}$  electrodes are shown in Fig. 5a and b. After cell discharge, large amounts of ORR aggregates ( $\text{Li}_2\text{O}_2$ ) were formed on the surface of the electrode (Fig. 5a). During the subsequent charge process, the ORR aggregates disappeared at a charge capacity of  $1,000\text{ mA h g}^{-1}$  (Fig. 5b), indicating the high reversibility of the  $\text{Fe}_3\text{O}_4\text{-Fe NH}$  electrode.

The impedance behavior of both the  $\text{Fe}_3\text{O}_4\text{-Fe NH}$  and  $\text{Fe}_3\text{O}_4\text{ NS}$  electrodes in fresh cells is almost the same, as shown in Fig. 5c–e. After the discharge process, the resistances of both the  $\text{Fe}_3\text{O}_4\text{-Fe NH}$  and  $\text{Fe}_3\text{O}_4\text{ NS}$  electrodes increase significantly, which is due to the generation of insulating ORR products ( $\text{Li}_2\text{O}_2$ ). Interestingly, after the charge process, the resistances of both electrodes are remarkably reduced (Fig. 5e), indicating that the formed insulating ORR products can be completely decomposed during the charge process, which is consistent with the SEM images of the  $\text{Fe}_3\text{O}_4\text{-Fe NH}$  electrode after the charge process (Fig. 5b).

A fitting model using equivalent circuits and the corresponding fitting values are depicted in Supplementary Table S3. In the Nyquist plots, the semicircle observed in the high-frequency region appears to be associated with film formation, mainly the accumulation of discharge products such as  $\text{Li}_2\text{O}_2$  and the formation of a solid electrolyte interphase (SEI) layer owing to electrolyte decomposition on the electrodes. The intercept of this semicircle with the  $Z_{\text{real}}$  axis in the high-frequency region represents the total resistance of the electrolyte, separator, and electrical contacts ( $R_c$ ), whereas the diameter of the semicircle represents the interfacial resistance ( $R_i$ ), which is related to the coverage of  $\text{Li}_2\text{O}_2$  and SEI layers. The semicircle in the medium-frequency region is associated with the time constant for charge-transfer resistance ( $R_{ct}$ ) at the electrode/electrolyte interface<sup>36</sup>. The  $\text{Fe}_3\text{O}_4\text{ NS}$  electrode has a significantly larger  $R_{ct}$  ( $2354.0\ \Omega\ \text{mg}^{-1}$ ) than the  $\text{Fe}_3\text{O}_4\text{-Fe NH}$  electrode ( $1151.8\ \Omega\ \text{mg}^{-1}$ ) at the open circuit voltage (OCV), suggesting that the highly conductive the  $\text{Fe}_3\text{O}_4\text{-Fe}$  nanohybrids



**Figure 5.** FESEM images of the  $\text{Fe}_3\text{O}_4\text{-Fe NH}$  electrode after (a) discharge and (b) charge process. Nyquist plots of the  $\text{Fe}_3\text{O}_4\text{-Fe NH}$  electrode and the  $\text{Fe}_3\text{O}_4\text{ NS}$  electrodes (c) at OCV, after (d) discharge process and (e) charge process. (f) Schematic representation emphasizing the electron transport paths through the metallic Fe.

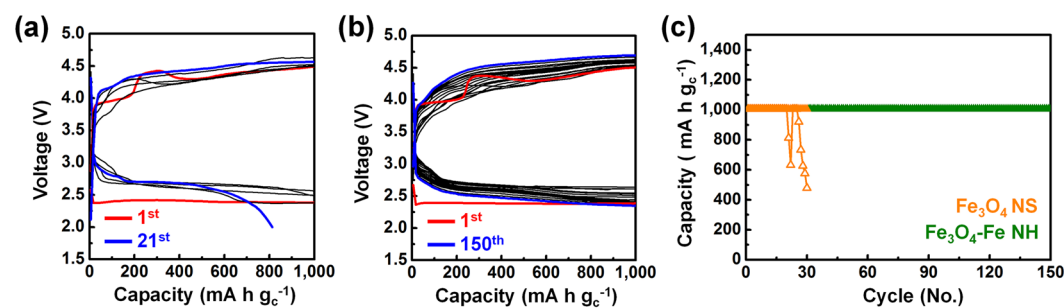


**Figure 6.** A high rate performances of the  $\text{Fe}_3\text{O}_4\text{-Fe NH}$  and the  $\text{Fe}_3\text{O}_4\text{ NS}$  electrode at a current rate of  $2,000\text{ mA g}^{-1}$ . (a) The  $\text{Fe}_3\text{O}_4\text{ NS}$  electrode and (b) the  $\text{Fe}_3\text{O}_4\text{-Fe NH}$  electrode at a fixed capacity regime of  $1,000\text{ mA h g}^{-1}$  with a rate of  $2,000\text{ mA g}^{-1}$ , (c) comparison of the discharge-charge specific capacity versus the cycle number of the  $\text{Fe}_3\text{O}_4\text{-Fe NH}$  electrode and the  $\text{Fe}_3\text{O}_4\text{ NS}$  electrodes.

decrease the electrode resistance. Similarly, the  $\text{Fe}_3\text{O}_4\text{-Fe NH}$  electrode has a significantly smaller  $R_{ct}$  than the  $\text{Fe}_3\text{O}_4\text{ NS}$  electrode after both the discharge and charge processes (see Supplementary Fig. S7).  $R_{ct}$  is inversely proportional to the rate coefficient of the chemical reaction, the porosity and the  $\text{O}_2$  concentration in the oxygen electrode. In  $\text{Li-O}_2$  battery, electrolytes should diffuse safely reduced oxygen species ( $\text{O}_2^-$  or  $\text{O}_2^{2-}$  by ORR:  $\text{O}_2 + ne^- \rightarrow \text{O}_2^{n-}$ ,  $n = 1$  or  $2$ ). As higher  $\text{O}_2$  concentration,  $R_{CT}$  is lower<sup>37–39</sup>. Decrease of  $R_{CT}$  indicates facilitated oxygen diffusion pathway and less agglomeration of the oxygen electrode. This means that the electrolyte and the electrode is activated. Therefore, the  $R_{CT}$  is remarkably reduced that the  $\text{Fe}_3\text{O}_4\text{-Fe NH}$  electrode is relatively stable cycling, and provide evidences for the superior performance of the  $\text{Fe}_3\text{O}_4\text{-Fe NH}$  electrode due to intimate contact and effective lithium ions and oxygen diffusion. Interestingly,  $R_i$  of the two electrodes show a similar tendency after discharging, and  $R_i$  of both electrodes disappear after the charging process of both electrodes due to sufficient OER activity, except for  $R_i$  after the first charge of the  $\text{Fe}_3\text{O}_4\text{ NS}$  electrode. This contributes to higher electronic conductivity, indicating the high ORR/OER activity of the  $\text{Fe}_3\text{O}_4\text{-Fe NH}$  electrode. We have evaluated the stability of Fe nanospheres through XPS. As shown in Supplementary Fig. S8, the Fe 2p XPS spectra of pristine  $\text{Fe}_3\text{O}_4\text{-Fe NH}$  electrode obviously indicate  $\text{Fe}^0$ . The Fe 2p peaks at approximately 707 eV and 720 eV are associated, with the  $\text{Fe}^0$  2p<sub>3/2</sub> and 2p<sub>1/2</sub> states of the Fe metal, respectively<sup>40</sup>. The Fe 2p peaks disappear after discharge process because it is covered by ORR products. After charge process, the Fe 2p peaks appear again. Therefore, it seems that even after discharge-charge cycling, relatively stable Fe remains rather than complete oxidation.

Additionally, another considerable improvement of the Fe<sub>3</sub>O<sub>4</sub>-Fe NH electrode is a high rate performance in a Li–O<sub>2</sub> battery, Fig. 6 show the galvanostatic discharge-charge cycling performance of the Fe<sub>3</sub>O<sub>4</sub>-Fe NH and Fe<sub>3</sub>O<sub>4</sub> NS electrodes obtained in the fixed capacity regime of 1,000 mA h g<sub>c</sub><sup>-1</sup> at a rate of 2,000 mA g<sub>c</sub><sup>-1</sup>. The Fe<sub>3</sub>O<sub>4</sub>-Fe NH electrode exhibited more stable cycling performance over 150 cycles compared to the Fe<sub>3</sub>O<sub>4</sub> NS electrode. The Fe<sub>3</sub>O<sub>4</sub> NS electrode exhibited a sudden deterioration of discharge capacity because its active sites were blocked by intrinsically electronically insulating ORR products, which could be confirmed again for electrode resistance problems (Fig. 5c–e). We note that the high catalytic activity of Fe<sub>3</sub>O<sub>4</sub>-Fe NH electrode, its result in an enhancement of the electronic conductivity, and it promote the decomposition of the insulating products.

## Conclusion

In this work, we fabricated the Fe<sub>3</sub>O<sub>4</sub>-Fe nanohybrid and the Fe<sub>3</sub>O<sub>4</sub> nanosphere electrocatalysts for Li–O<sub>2</sub> batteries via the electrical wire pulse process. The obtained the Fe<sub>3</sub>O<sub>4</sub>-Fe nanohybrids featured 0D spheres deposited on 2D flake composites, good dispersibility, and electronic conductivity. In Li–O<sub>2</sub> battery tests at a current rate of 500 mA g<sub>c</sub><sup>-1</sup>, the Fe<sub>3</sub>O<sub>4</sub>-Fe nanohybrids had a low overpotential of 1.39 V, a high capacity of 13,890 mA h g<sub>c</sub><sup>-1</sup>, and stable cycling over 100 cycles at a fixed capacity of 1,000 mA h g<sub>c</sub><sup>-1</sup>. Importantly, a comparison of the EIS results for the Fe<sub>3</sub>O<sub>4</sub>-Fe NH and Fe<sub>3</sub>O<sub>4</sub> NS electrodes demonstrates the origin of the good ORR/OER activity.

## Method

**Materials and synthesis.** Commercial Fe wire (0.2 mm in diameter) was purchased Nano Tech (Korea), and electrical pulse equipment (NTi-mini P, Nano Tech, Korea) was used to fabricate the Fe<sub>3</sub>O<sub>4</sub>-Fe nanohybrids and the Fe<sub>3</sub>O<sub>4</sub> nanospheres. As a similar process reported in previous works<sup>25, 26</sup>, Fe-based aqueous nanocolloidal suspension could be successfully obtained. After completing the electrical wire pulse process with Fe wire, the obtained nanocolloidal suspension was allowed to settle for 3 days and divided into two classes of colloidal suspensions. Then, the selected nanocolloidal suspension was sonicated and filtered through a nylon membrane (Durapore, 0.22 mm, Millipore) several times, and subsequently dried at 120 °C for 8 hr.

**Characterization of Fe<sub>3</sub>O<sub>4</sub>-Fe nanohybrids and Fe<sub>3</sub>O<sub>4</sub> nanospheres.** The morphology and composition of the Fe<sub>3</sub>O<sub>4</sub>-Fe nanohybrids and the Fe<sub>3</sub>O<sub>4</sub> nanospheres were investigated using transmission electron microscopy (TEM; Tecnai G2 F30 S-Twin, FEI), high angle annular dark field-scanning transmission electron microscopy with energy-dispersive X-ray spectroscopy (HAADF-STEM with EDS; JEM-2100F, JEOL, USA), field emission scanning electron microscopy (FESEM; S-4300, Hitachi), and X-ray photo-electron spectroscopy (XPS; PHI X-tool, ULVAC-PHI, Japan). The phase and crystal structure were characterized by X-ray diffraction (XRD; Ultima III, Rigaku). The particle size distribution was determined from dynamic light scattering (DLS) analyses using a particle size analyzer (PSA; ELSZ-1000, Otsuka Electronics Korea Co. Ltd.).

**Electrochemical performance of Li–O<sub>2</sub> cells.** The electrochemical performance of the Fe<sub>3</sub>O<sub>4</sub> nanospheres and the Fe<sub>3</sub>O<sub>4</sub>-Fe nanohybrids was evaluated using Swagelok-type cells. The electrode was prepared by mixing each Fe nanopowder (45%) with Super P carbon black (45%) and carboxymethyl cellulose (10%; CMC, Aldrich, Average Mw ~700,000). The obtained slurry was spread onto nickel foam, and the loading weight of the electrode was adjusted to above 0.2 mg of super P carbon black per cm<sup>2</sup>. The Li–O<sub>2</sub> cells were assembled in an Ar-filled glove box. The cells consisted of a lithium foil as the anode, a glass microfiber filter (Celgard 2400, Wellcos) as the separator, 1 M LiNO<sub>3</sub> (Alfa Aesar, anhydrous, ≥99.999%) in N,N-dimethylacetamide (DMAc; Alfa Aesar, anhydrous, ≥99.8%) as the electrolyte, the electrode, and carbon cloth (W0S1002, CeTech) as a gas diffusion layer. All measurements were conducted in 1.5 atm dry oxygen to avoid any negative effects of humidity and CO<sub>2</sub>. The assembled cells were tested with an automatic battery cyler (WBCS 3000, WonAtech) in a voltage window of 2.0–4.8 V. Electrochemical impedance spectroscopy (EIS) was performed with an electrochemical workstation (Ivium-n-Stat electrochemical analyzer, Ivium Technologies B. V.). The impedance response was collected by applying AC voltages of 10 mV while maintaining a constant DC voltage in the frequency range of 0.01 Hz to 100 kHz. All the above measurements were conducted at room temperature.

## References

1. Wang, H. *et al.* Y. Bifunctional non-noble metal oxide nanoparticle electrocatalysts through lithium-induced conversion for overall water splitting. *Nat. Commun.* **6**, 7261 (2015).
2. Chen, Z., Higgins, D., Yu, A. P., Zhang, L. & Zhang, J. A Review on non-precious metal electrocatalysts for PEM fuel cells. *Energy Environ. Sci.* **4**, 3167–3192 (2011).
3. Arena, F., Chio, R. D., Gumina, B., Spadaro, L. & Trunfio, G. Recent advances on wet air oxidation catalysts for treatment of industrial wastewaters. *Inorg. Chim. Acta* **431**, 101–109 (2015).
4. Kalia, S. *et al.* Magnetic polymer nanocomposites for environmental and biomedical applications. *Colloid Polym. Sci.* **292**, 2025–2052 (2014).
5. Roy, P. & Srivastava, S. K. Nanostructured anode materials for lithium ion batteries. *J. Mater. Chem. A.* **3**, 2454–2484 (2015).
6. Ellis, B. L., Knauth, P. & Djenizian, T. Three-dimensional self-supported metal oxides for advanced energy storage. *Adv. Mater.* **26**, 3368–3397 (2014).
7. Park, M., Sun, H., Lee, H., Lee, J. & Cho, J. Lithium-air batteries: survey on the current status and perspectives towards automotive applications from a battery industry standpoint. *Adv. Energy Mater.* **2**, 780–800 (2012).
8. Capsoni, D., Bini, M., Ferrari, S., Quartarone, E. & Mustarelli, P. Recent advances in the development of Li–air Batteries. *J. Power Sources* **220**, 253–263 (2012).
9. Park, M.-S. *et al.* Porous nanoarchitectures of spinel-type transition metal oxides for electrochemical energy storage systems. *Phys. Chem. Chem. Phys.* **17**, 30963–30977 (2015).
10. Jung, K.-N. *et al.* Rechargeable lithium-air batteries: a perspective on the development of oxygen electrodes. *J. Mater. Chem. A.* **4**, 14050–14068 (2016).
11. Lu, Y. *et al.* Lithium–oxygen batteries: bridging mechanistic understanding and battery performance. *Energy Environ. Sci.* **6**, 750–768 (2013).



12. Li, F., Zhang, T. & Zhou, H. Challenges of non-aqueous Li–O<sub>2</sub> batteries: electrolytes, catalysts, and anodes. *Energy Environ. Sci.* **6**, 1125–1141 (2013).
13. Shao, Y. *et al.* Making Li–air batteries rechargeable: material challenges. *Adv. Funct. Mater.* **23**, 987–1004 (2013).
14. Radin, M. D., Monroe, C. W. & Siegel, D. J. Impact of space–charge layers on sudden death in Li/O<sub>2</sub> batteries. *J. Phys. Chem. Lett.* **6**, 3017–3022 (2015).
15. Viswanathan, W. *et al.* Electrical conductivity in Li<sub>2</sub>O<sub>2</sub> and its role in determining capacity limitations in non-aqueous Li–O<sub>2</sub> batteries. *J. Chem. Phys.* **135**, 214704 (2011).
16. Uddin, M. A., Tsuda, H., Wu, S. & Sasaoka, E. Catalytic decomposition of biomass tars with iron oxide catalysts. *Fuel* **87**, 451–459 (2008).
17. Li, X. *et al.* Hierarchically structured Fe<sub>3</sub>O<sub>4</sub> microspheres: morphology control and their application in wastewater treatment. *CrystEngComm* **13**, 642–648 (2011).
18. Zhang, Y. *et al.* Synthesis of mesoporous carbon capsules encapsulated with magnetite nanoparticles and their application in wastewater treatment. *J. Mater. Chem.* **21**, 3664–3671 (2011).
19. Davis, B. H. Fischer-tropsch synthesis: Reaction mechanisms for iron catalysts. *Catalysis Today* **141**, 25–33 (2009).
20. Vago, E. R. & Calvo, E. J. Electrocatalysis of oxygen reduction at Fe<sub>3</sub>O<sub>4</sub> oxide electrodes in alkaline solutions. *J. Electroanal. Chem.* **339**, 41–67 (1992).
21. Lv, H., Jiang, R., Zhang, X., Wang, J. & Li, Y. A Novel litchi–like Fe<sub>3</sub>O<sub>4</sub>/graphene composite catalyst for the lithium-air battery. *Int. J. Electrochem. Sci.* **10**, 7622–7630 (2015).
22. Lv, H., Jiang, R., Li, Y., Zhang, X. & Wang, J. Microemulsion-mediated hydrothermal growth of pagoda–like Fe<sub>3</sub>O<sub>4</sub> microstructures and their application in a lithium–air battery. *Ceram. Int.* **41**, 8843–8848 (2015).
23. Lu, J. *et al.* Synthesis and characterization of uniformly dispersed Fe<sub>3</sub>O<sub>4</sub>/Fe nanocomposite on porous carbon: application for rechargeable Li–O<sub>2</sub> batteries. *RSC Adv.* **3**, 8276–8285 (2013).
24. Wang, F., Wu, X., Shen, C. & Wen, Z. Facile synthesis of Fe@Fe<sub>2</sub>O<sub>3</sub> core-shell nanowires as O<sub>2</sub> electrode for high-energy Li–O<sub>2</sub> batteries. *J. Solid State Electrochem.* **20**, 1831–1836 (2016).
25. Jee, S.-W. *et al.* Enhanced oxygen reduction and evolution by In-situ decoration of hematite nanoparticles on carbon nanotube cathode for high-capacity nonaqueous lithium-oxygen batteries. *J. Mater. Chem. A* **3**, 13767–13775 (2015).
26. Danwittayakul, S., Lakshman, K., Al-Harhi, S. & Dutta, J. Enhanced hydrogen selectivity via photo–engineered surface defects for methanol steam reformation using zinc oxide–copper nanocomposite catalysts. *Applied Catalysis A: General* **471**, 63–69 (2014).
27. Gao, G. *et al.* Gram scale synthesis of superparamagnetic Fe<sub>3</sub>O<sub>4</sub> nanoparticles and fluid via a facile solvothermal route. *CrystEngComm* **13**, 1782–1785 (2011).
28. Wan, D., Li, W., Wang, G. & Wei, X. Shape-controllable synthesis of peroxidase-like Fe<sub>3</sub>O<sub>4</sub> nanoparticles for catalytic removal of organic pollutants. *J. Mater. Eng. Perform.* **25**, 4333–4340 (2016).
29. Lee, D. H., Shim, H. W. & Kim, D. W. Facile synthesis of heterogeneous Ni-Si@C nanocomposites as high-performance anodes for Li–ion batteries. *Electrochim. Acta* **146**, 60–67 (2014).
30. Lee, D. H., Seo, S. D., Lee, G. H., Hong, H. S. & Kim, D. W. One-pot synthesis of Fe<sub>3</sub>O<sub>4</sub>/Fe/MWCNT nanocomposites via electrical wire pulse for Li ion battery electrodes. *J. Alloys. Comp.* **606**, 204–207 (2014).
31. Zhang, J., Huang, F. & Lin, Z. Progress of nanocrystalline growth kinetics based on oriented attachment. *Nanoscale* **2**, 18–34 (2010).
32. Zhu, J., Li, D., Jiang, D. & Chen, M. Facile synthesis and characterization of hexagonal magnetite nanoplates. *Micro Nano Lett.* **8**, 383–385 (2013).
33. Kang, S. J., Mori, T., Narizuka, S., Wilcke, W. & Kim, H. C. Deactivation of carbon electrode for elimination of carbon dioxide evolution from rechargeable lithium–oxygen cells. *Nat. Commun.* **5**, 3937 (2014).
34. Sun, B., Huang, X. D., Chen, S. Q., Zhang, J. Q. & Wang, G. X. An Optimized LiNO<sub>3</sub>/DMSO electrolyte for high-performance rechargeable Li–O<sub>2</sub> batteries. *RSC Adv.* **4**, 11115–11120 (2014).
35. Ganapathy, S. *et al.* Nature of Li<sub>2</sub>O<sub>2</sub> oxidation in a Li–O<sub>2</sub> battery revealed by operando X-ray diffraction. *J. Am. Chem. Soc.* **136**, 16335–16344 (2014).
36. Kalubarme, R. S. *et al.* Simple synthesis of highly catalytic carbon-free MnCo<sub>2</sub>O<sub>4</sub>@Ni as an oxygen electrode for rechargeable Li–O<sub>2</sub> batteries with long-term stability. *Sci. Rep.* **5**, 13266 (2015).
37. Liu, C. *et al.* High energy and power density Li–O<sub>2</sub> battery cathodes based on amorphous RuO<sub>2</sub> loaded carbon free and binderless nickel nanofoam architectures. *RSC Adv.* **6**, 81712–81718 (2016).
38. Zhang, G. Q. *et al.* α-MnO<sub>2</sub>/carbon nanotube/carbon nanofiber composite catalytic air Electrodes for rechargeable lithium-air batteries. *J. Electrochem. Soc.* **158**, A822–A827 (2011).
39. Zhang, G. Q. *et al.* Lithium–air batteries using SWNT/CNT buckypapers as air electrodes. *J. Electrochem. Soc.* **157**, A953–A956 (2010).
40. Fang, H. *et al.* Magnetic and electrical properties of ε-Fe<sub>3</sub>N on c-plane GaN. *J. Phys. D: Appl. Phys.* **45**, 315002 (2012).

## Acknowledgements

This work was supported by the National Research Foundation of Korea (NRF) Grant funded by the Ministry of Science, ICT, and Future Planning (No. 2016R1A2B2012728, 2016M3A7B4909318) and by the Korea Research Institute of Chemical Technology (KRICT cooperation project). The authors extend their appreciation to the International Scientific Partnership Program ISPP at King Saud University for funding this research work through ISPP# 0076).

## Author Contributions

S.L. performed, analyzed the experiments. G.H.L. performed theoretical analysis and drafted the manuscript. H.J.L. participated in electrochemical tests. M.A.D. analyzed the results of electrochemical properties. D.W.K. conceived and designed the study, led the discussion of the results, and performed the final edits of the manuscript. All authors made critical contributions to the work, discussed the results and commented on the manuscript.

## Additional Information

**Supplementary information** accompanies this paper at doi:[10.1038/s41598-017-09982-9](https://doi.org/10.1038/s41598-017-09982-9)

**Competing Interests:** The authors declare that they have no competing interests.

**Publisher's note:** Springer Nature remains neutral with regard to jurisdictional claims in published maps and institutional affiliations.





**Open Access** This article is licensed under a Creative Commons Attribution 4.0 International License, which permits use, sharing, adaptation, distribution and reproduction in any medium or format, as long as you give appropriate credit to the original author(s) and the source, provide a link to the Creative Commons license, and indicate if changes were made. The images or other third party material in this article are included in the article's Creative Commons license, unless indicated otherwise in a credit line to the material. If material is not included in the article's Creative Commons license and your intended use is not permitted by statutory regulation or exceeds the permitted use, you will need to obtain permission directly from the copyright holder. To view a copy of this license, visit <http://creativecommons.org/licenses/by/4.0/>.

© The Author(s) 2017